



# On maximum enstrophy dissipation in 2D Navier–Stokes flows in the limit of vanishing viscosity

Pritpal Matharu<sup>a,1</sup>, Bartosz Protas<sup>a,\*</sup>, Tsuyoshi Yoneda<sup>b</sup>

<sup>a</sup> Department of Mathematics and Statistics, McMaster University, Hamilton, ON, Canada

<sup>b</sup> Graduate School of Economics, Hitotsubashi University, 2-1 Naka, Kunitachi, Tokyo 186-8601, Japan

## ARTICLE INFO

### Article history:

Received 7 June 2022

Received in revised form 22 August 2022

Accepted 28 August 2022

Available online 10 September 2022

Communicated by J. Gibbon

### Keywords:

2D Navier–Stokes equation

Enstrophy dissipation

Inviscid limit

PDE-constrained optimization

## ABSTRACT

We consider enstrophy dissipation in two-dimensional (2D) Navier–Stokes flows and focus on how this quantity behaves in the limit of vanishing viscosity. After recalling a number of a priori estimates providing lower and upper bounds on this quantity, we state an optimization problem aimed at probing the sharpness of these estimates as functions of viscosity. More precisely, solutions of this problem are the initial conditions with fixed palinstrophy and possessing the property that the resulting 2D Navier–Stokes flows locally maximize the enstrophy dissipation over a given time window. This problem is solved numerically with an adjoint-based gradient ascent method and solutions obtained for a broad range of viscosities and lengths of the time window reveal the presence of multiple branches of local maximizers, each associated with a distinct mechanism for the amplification of palinstrophy. The dependence of the maximum enstrophy dissipation on viscosity is shown to be in quantitative agreement with the estimate due to Ciampa et al. (2021), demonstrating the sharpness of this bound.

© 2022 Elsevier B.V. All rights reserved.

## Contents

1. Introduction.....	1
2. Optimization problem.....	3
3. Solution approach.....	3
3.1. Gradient-based optimization.....	3
3.2. Computational approach.....	4
4. Results.....	5
5. Summary and conclusions.....	7
Declaration of competing interest.....	8
Acknowledgments.....	8
Appendix A. Supplementary data.....	8
References.....	8

## 1. Introduction

The physical phenomenon of “anomalous dissipation”, also referred to as the “zeroth law of turbulence”, is one of the oldest problems in turbulence [1]. This empirical law states that the energy dissipation in either forced or decaying three-dimensional (3D) turbulent flows approaches a nonzero limit as the fluid viscosity  $\nu > 0$  vanishes, with all other flow parameters remaining fixed. There is a lot of evidence coming from both experiments

and numerical simulations supporting this anomalous behavior of the energy dissipation [2,3], but we are still far from being able to understand this problem from the mathematical point of view. The main consequence of the dissipation anomaly is an unbounded increase of velocity gradients which would in turn imply finite-time singularities in solutions of the inviscid Euler equations [4]. Similar dissipation anomalies are also known to occur in the behavior of passive scalars [5,6].

Dissipation anomaly arises in solutions of the one-dimensional (1D) Burgers equation [7]. As regards 2D flows, the relevant question is about the behavior of the enstrophy dissipation in the limit of vanishing viscosity. The assumption that enstrophy dissipation tends to a finite (nonzero) limit as  $\nu \rightarrow 0$  underlaid Batchelor's theory of 2D turbulence [8]. However, in [9] it was

\* Corresponding author.

E-mail address: [bprotas@mcmaster.ca](mailto:bprotas@mcmaster.ca) (B. Protas).

<sup>1</sup> International Research Fellow of the Japan Society for the Promotion of Science (Graduate Fellowships for Research in Japan).

argued that this quantity in fact vanishes in the inviscid limit such that Navier–Stokes flows in 2D are not subject to dissipation anomaly. This result was confirmed by rigorous analysis of the inviscid limit of 2D Navier–Stokes flows [10].

While there is no dissipation anomaly in 2D flows, it is interesting to know the worst-case (slowest) rate at which the enstrophy dissipation vanishes in the limit  $\nu \rightarrow 0$ . A number of theoretical results, in the form of both lower and upper bounds on the dependence of the enstrophy dissipation on  $\nu$ , have been established and are reviewed below. The goal of the present study is to address this question computationally by finding flows with the largest possible enstrophy dissipation as the viscosity vanishes. Such “extreme” flows will be found by solving suitably defined optimization problems with constraints in the form of partial differential equations (PDEs). This will provide insights about the sharpness of various rigorous bounds on the enstrophy dissipation in the inviscid limit. While methods of PDE optimization have had a long history in various applied areas [11], they have recently been employed to study certain fundamental problems concerning extreme behavior in fluid mechanics [12]. In particular, problems somewhat related to the subject of the present study were investigated using such techniques in [13–15].

We consider the incompressible Navier–Stokes system on a 2D periodic domain  $\Omega := \mathbb{T}^2 = [0, 1]^2$  (“=” means “equal to by definition”) which can be written in the vorticity form as

$$\frac{\partial \omega_\nu}{\partial t} + \nabla^\perp \psi_\nu \cdot \nabla \omega_\nu = \nu \Delta \omega_\nu \quad \text{in } \Omega \times (0, T], \tag{1a}$$

$$-\Delta \psi_\nu = \omega_\nu \quad \text{in } \Omega \times (0, T], \tag{1b}$$

$$\omega_\nu(t = 0) = \varphi \quad \text{in } \Omega, \tag{1c}$$

where  $\omega_\nu$  and  $\psi_\nu$  are the vorticity component perpendicular to the plane of motion and the corresponding streamfunction, both assumed to satisfy the periodic boundary conditions in the space variable  $\mathbf{x}$ , whereas  $T > 0$  is the length of the time window considered. The symbol  $\varphi$  denotes the initial condition which without loss of generality is assumed to have zero mean, i.e.,

$$\int_\Omega \varphi(\mathbf{x}) \, d\mathbf{x} = 0. \tag{2}$$

Problem (1) is known to be globally well-posed in the classical sense [16]. Its solutions are characterized by the enstrophy and palinstrophy defined, respectively, as<sup>2</sup>

$$\mathcal{E}(\omega_\nu(\cdot, t)) := \frac{1}{2} \int_\Omega |\omega_\nu(\mathbf{x}, t)|^2 \, d\mathbf{x}, \tag{3}$$

$$\mathcal{P}(\omega_\nu(\cdot, t)) := \frac{1}{2} \int_\Omega |\nabla \omega_\nu(\mathbf{x}, t)|^2 \, d\mathbf{x}, \tag{4}$$

which satisfy the relation

$$\frac{d\mathcal{E}(t)}{dt} = -2\nu \mathcal{P}(t). \tag{5}$$

We then define our main quantity of interest as

$$\begin{aligned} \chi_\nu(\varphi) &:= \frac{2\nu}{T} \int_0^T \mathcal{P}(t) \, dt = \frac{\nu}{T} \int_0^T \int_\Omega |\nabla \omega_\nu(\mathbf{x}, t; \varphi)|^2 \, d\mathbf{x} \, dt \\ &= \frac{\mathcal{E}(0) - \mathcal{E}(T)}{T}, \end{aligned} \tag{6}$$

which represents the enstrophy dissipation per unit of time and will be viewed here as a function of the initial data  $\varphi$ .

<sup>2</sup> For consistency with the convention used in our earlier studies, cf. [12], both these quantities are defined with a factor of 1/2. Without the risk of confusion we will sometimes use the simplified notation  $\mathcal{E}(t) = \mathcal{E}(\omega_\nu(\cdot, t))$  and  $\mathcal{P}(t) = \mathcal{P}(\omega_\nu(\cdot, t))$ .

The enstrophy dissipation (6) has been the subject of numerous estimates. For technical reasons we will hereafter assume that  $0 < \nu < 1$ . We refer to the following result as a “conjecture” since it relies on some assumptions, albeit well justified, about the form of the spectrum of the solutions of (1).

**Conjecture 1** (Tran & Dritschel [9]). *The enstrophy dissipation in solutions of system (1) is bounded above by*

$$\chi_\nu \leq C [-\ln(\nu)]^{-\frac{1}{2}}, \tag{7}$$

for some constant  $C > 0$  depending on the initial condition  $\varphi$  and the length  $T$  of the time window.

Hereafter  $C = C(T)$  will denote a generic positive constant depending on the length  $T$  of the considered time window with numerical values differing from one instant to another.

Bounds on enstrophy dissipation are closely related to another problem which has recently received considerable attention, namely, the question of the convergence as  $\nu \rightarrow 0$  of Navier–Stokes flows to solutions of the inviscid Euler equations obtained by setting  $\nu = 0$  in (1a) and corresponding to the same initial condition  $\varphi$ . More specifically, noting (5), the fact that solutions of the inviscid Euler system conserve the enstrophy and using the reverse triangle inequality, we have

$$\begin{aligned} \chi_\nu(\varphi) &= \frac{\nu}{T} \int_0^T \|\nabla \omega_\nu(\mathbf{x}, t; \varphi)\|_{L^2(\Omega)}^2 \, dt = \frac{2\nu}{T} \int_0^T \mathcal{P}(t) \, dt \\ &= \frac{1}{T} [\mathcal{E}(0) - \mathcal{E}(T)] = \frac{1}{T} \left[ \|\varphi\|_{L^2(\Omega)}^2 - \|\omega_\nu(\mathbf{x}, T; \varphi)\|_{L^2(\Omega)}^2 \right] \\ &= \frac{1}{T} \left[ \|\omega(\mathbf{x}, T; \varphi)\|_{L^2(\Omega)}^2 - \|\omega_\nu(\mathbf{x}, T; \varphi)\|_{L^2(\Omega)}^2 \right] \\ &\leq \frac{1}{T} \left[ \|\omega(\mathbf{x}, T; \varphi)\|_{L^2(\Omega)} + \|\omega_\nu(\mathbf{x}, T; \varphi)\|_{L^2(\Omega)} \right] \\ &\quad \times \|\omega(\mathbf{x}, T; \varphi) - \omega_\nu(\mathbf{x}, T; \varphi)\|_{L^2(\Omega)} \\ &\leq \frac{2}{T} \|\varphi\|_{L^2(\Omega)} \|\omega(\mathbf{x}, T; \varphi) - \omega_\nu(\mathbf{x}, T; \varphi)\|_{L^2(\Omega)}, \end{aligned} \tag{8}$$

where  $\omega(\mathbf{x}, t) := \omega_0(\mathbf{x}, t)$  denotes the vorticity in the inviscid Euler flow. The above relation shows that the enstrophy dissipation over the time window  $[0, T]$  can be bounded from above in terms of the difference of the vorticity fields in the viscous and inviscid flows obtained with the same initial data  $\varphi$  at time  $t = T$ . Quantifying this difference in terms of viscosity as  $\nu \rightarrow 0$  has been the subject of some recent studies. In [17] the authors showed the strong convergence of  $\omega_\nu$  to  $\omega$  as  $\nu \rightarrow 0$  when  $\varphi \in L^\infty(\Omega)$ , implying the vanishing of the right-hand side (RHS) in (8). Moreover, the following estimate was established in the case when  $\varphi \in L^\infty(\Omega) \cap B_{2,\infty}^s(\Omega)$  for some  $s > 0$ , where  $L^p$  and  $B_{p,q}^s$  are the usual Lebesgue and Besov spaces,

$$\sup_{t \in [0, T]} \|\omega(\cdot, t) - \omega_\nu(\cdot, t)\|_{L^p(\Omega)} \leq C(\nu T)^{\frac{s-2CTM}{p(1+s e^{-CTM})}}, \tag{9}$$

where  $M := \|\varphi\|_{L^\infty(\Omega)}$ . This problem was revisited in [18] where it was proved that

$$\begin{aligned} &\sup_{t \in [0, T]} \|\omega(\cdot, t) - \omega_\nu(\cdot, t)\|_{L^p(\Omega)} \\ &\leq C M^{1-\frac{1}{p}} \max \left\{ \phi_{\varphi,p,M} \left( C \nu^{\frac{e^{-CT}}{2}} \right), \left( C \nu^{\frac{e^{-CT}}{2}} \right)^{\frac{e^{-CT}}{2p}} \right\}, \end{aligned} \tag{10}$$

where now  $C = C(T, M)$  and  $\phi_{\varphi,p,M} : \mathbb{R}^+ \rightarrow \mathbb{R}^+$  is a continuous function such that  $\phi_{\varphi,p,M}(0) = 0$ . Additional results were also obtained recently in [19,20]. In particular, the following bound was produced in [20], which improves the rate of the weak

convergence of  $\omega_\nu$  to  $\omega$  as  $\nu \rightarrow 0$ ,

$$\sup_{t \in [0, T]} \|\omega(\cdot, t) - \omega_\nu(\cdot, t)\|_{\dot{H}^{-1}(\Omega)} \leq C \left[ \frac{\nu}{|\ln(\nu)|} \right]^{\frac{e^{-CT}}{2}}. \quad (11)$$

We reiterate that, in the light of relation (8), inequalities (9)–(10) imply viscosity-dependent upper bounds on the enstrophy dissipation (6). This is not the case for estimate (11) as it involves a weaker norm than in (8). We will nonetheless refer to this estimate when we discuss our results in Section 4 with the hope that our findings may inspire further work on refining this estimate. On the other hand, as is evident from the following theorem, a lower bound on the maximum enstrophy dissipation is also available.

**Theorem 1** (Jeong & Yoneda [21]). *Let  $\omega_\nu$  be the unique solution to (1). Then, there exists initial data  $\varphi$  such that the enstrophy dissipation is bounded below by*

$$\chi_\nu \geq C\nu [-\ln(\nu)]^{\frac{1}{2}}. \quad (12)$$

Upper bounds on the energy and enstrophy dissipation in 2D Navier–Stokes flows in the presence of external forcing were obtained in [22].

In the present study we construct families of 2D Navier–Stokes flows which at fixed values of the viscosity  $\nu$  locally maximize the enstrophy dissipation  $\chi_\nu$  over the prescribed time window  $[0, T]$ . These flows are found using methods of numerical optimization to solve PDE-constrained optimization problems in which the enstrophy dissipation (6) is maximized with respect to the initial condition  $\varphi$  in (1) subject to certain constraints. This is a non-convex optimization problem and we demonstrate that for every pair  $\nu$  and  $T$  it admits several branches of locally maximizing solutions, each corresponding to a distinct dynamic mechanism for amplification of palinstrophy (which, as is evident from (5), drives the dissipation of enstrophy). Finally, by assessing the dependence of the maximum enstrophy dissipation determined in this way for fixed  $T$  on the viscosity for decreasing values of  $\nu$ , we arrive at interesting new insights about the sharpness of the different a priori estimates discussed above.

The structure of the paper is as follows: in the next section we introduce the optimization problem formulated to maximize the enstrophy dissipation whereas in Section 3 we outline our gradient-based approach to finding families of local maximizers of that problem; computational results are presented in Section 4 whereas discussion and final conclusions are deferred to the last section.

## 2. Optimization problem

Given a fixed viscosity  $\nu$  and length  $T$  of the time window, we aim to construct flows maximizing the enstrophy dissipation  $\chi_\nu$  which will be accomplished by finding suitable optimal initial conditions  $\check{\varphi}_\nu^T$  in system (1). Since the enstrophy dissipation is given in terms of a time integral of the palinstrophy, cf. (6), we will restrict our attention to initial data with bounded palinstrophy  $\mathcal{P}_0 := \mathcal{P}(\varphi)$ , even though system (1) admits classical solutions for a much broader class of initial data [16]. We thus have the following optimization problem.

**Problem 1.** Given  $\mathcal{P}_0, \nu, T > 0$  in system (1) and the objective functional (6), find

$$\check{\varphi}_\nu^T = \arg \max_{\varphi \in \mathcal{S}} \chi_\nu(\varphi), \quad \text{where}$$

$$\mathcal{S} := \left\{ \varphi \in H^1(\Omega) : \int_\Omega \varphi(\mathbf{x}) \, d\mathbf{x} = 0, \mathcal{P}(\varphi) = \mathcal{P}_0 \right\}.$$

The Sobolev space  $H^1(\Omega)$  is endowed with the inner product

$$\forall p_1, p_2 \in H^1(\Omega) \quad \langle p_1, p_2 \rangle_{H^1(\Omega)} = \int_\Omega p_1 p_2 + \ell^2 \nabla p_1 \cdot \nabla p_2 \, d\mathbf{x}, \quad (13)$$

where  $\ell \in \mathbb{R}^+$  is a parameter. We note that the inner products in (13) corresponding to different values of  $\ell$  are equivalent as long as  $0 < \ell < \infty$ . However, as will be shown in the next section, the choice of the parameter  $\ell$  plays an important role in the numerical solution of Problem 1. With the initial palinstrophy  $\mathcal{P}_0$  fixed, we will find families of locally maximizing solutions of Problem 1 parameterized by  $T$  for a range of viscosities  $\nu$ . Our approach to finding such local maximizers is described next.

## 3. Solution approach

### 3.1. Gradient-based optimization

Since Problem 1 is designed to test certain subtle mathematical properties of system (1), we choose to formulate the solution approach in the continuous (“optimize-then-discretize”) setting, where the optimality conditions, constraints and gradient expressions are derived based on the original PDE before being discretized for the purpose of numerical evaluation, instead of the alternative “discretize-then-optimize” approach often used in applications [11]. We first describe the discrete gradient flow focusing on computation of the gradient of the objective functional  $\chi_\nu(\varphi)$  with respect to the initial condition  $\varphi$  and then provide some details about numerical approximations.

For given values of  $\mathcal{P}_0, \nu$  and  $T$ , a local maximizer  $\check{\varphi}_\nu^T$  of Problem 1 can be found as  $\check{\varphi}_\nu^T = \lim_{n \rightarrow \infty} \varphi^{(n)}$  using the following iterative procedure representing a discretization of a gradient flow projected on  $\mathcal{S}$

$$\begin{aligned} \varphi^{(n+1)} &= \mathbb{P}_\mathcal{S} \left( \varphi^{(n)} + \tau_n \nabla \chi_\nu(\varphi^{(n)}) \right), \\ \varphi^{(1)} &= \varphi_0, \end{aligned} \quad (14)$$

where  $\varphi^{(n)}$  is an approximation of the maximizer obtained at the  $n$ th iteration,  $\varphi_0$  is the initial guess assumed to have zero mean and  $\tau_n$  is the length of the step in the direction of the gradient  $\nabla \chi_\nu(\varphi^{(n)})$ . The palinstrophy constraint is enforced by application of a projection operator  $\mathbb{P}_\mathcal{S} : H^1(\Omega) \rightarrow \mathcal{S}$  to be defined below. We defer discussion of the choice of the initial guess  $\varphi_0$  to the end of this subsection.

A key step in procedure (14) is evaluation of the gradient  $\nabla \chi_\nu(\varphi)$  of the objective functional  $\chi_\nu(\varphi)$ , cf. (6), representing its (infinite-dimensional) sensitivity to perturbations of the initial condition  $\varphi$ , and it is essential that the gradient be characterized by the required regularity, namely,  $\nabla \chi_\nu(\varphi) \in H^1(\Omega)$ . This is, in fact, guaranteed by the Riesz representation theorem [23] applicable because the Gâteaux (directional) differential  $\chi'_\nu(\varphi; \cdot) : H^1(\Omega) \rightarrow \mathbb{R}$ , defined as  $\chi'_\nu(\varphi; \varphi') := \lim_{\epsilon \rightarrow 0} \epsilon^{-1} [\chi_\nu(\varphi + \epsilon \varphi') - \chi_\nu(\varphi)]$  for some perturbation  $\varphi' \in H^1(\Omega)$ , is a bounded linear functional on  $H^1(\Omega)$ . The Gâteaux differential can be computed directly to give

$$\begin{aligned} \chi'_\nu(\varphi; \varphi') &= \frac{2\nu}{T} \int_0^T \int_\Omega \nabla \omega_\nu(\mathbf{x}, t; \varphi) \cdot \nabla \omega'_\nu(\mathbf{x}, t; \varphi, \varphi') \, d\mathbf{x} dt \\ &= - \frac{2\nu}{T} \int_0^T \int_\Omega \Delta \omega_\nu(\mathbf{x}, t; \varphi) \omega'_\nu(\mathbf{x}, t; \varphi, \varphi') \, d\mathbf{x} dt, \end{aligned} \quad (15)$$

where the last equality follows from integration by parts and the perturbation field  $\omega'_\nu = \omega'_\nu(\mathbf{x}, t; \varphi, \varphi')$  is a solution of the Navier–Stokes (1) system linearized around the trajectory corresponding

to the initial data  $\varphi$  [11], i.e.,

$$\begin{aligned} \mathcal{K} \begin{bmatrix} \omega'_v \\ \psi'_v \end{bmatrix} &:= \begin{bmatrix} \frac{\partial \omega'_v}{\partial t} + \nabla^\perp \psi'_v \cdot \nabla \omega_v + \nabla^\perp \psi_v \cdot \nabla \omega'_v - \nu \Delta \omega'_v \\ \Delta \psi'_v + \omega'_v \end{bmatrix} \\ &= \begin{bmatrix} 0 \\ 0 \end{bmatrix}, \end{aligned} \tag{16a}$$

$$\omega'_v(t = 0) = \varphi', \tag{16b}$$

which is subject to the periodic boundary conditions and where  $\psi'_v$  is the perturbation of the stream function  $\psi_v$ . The Riesz representation theorem then allows us to write

$$\chi'_v(\varphi; \varphi') = \left\langle \nabla \chi_v(\varphi), \varphi' \right\rangle_{H^1(\Omega)} = \left\langle \nabla^{L^2} \chi_v(\varphi), \varphi' \right\rangle_{L^2(\Omega)}, \tag{17}$$

where the  $L^2$  inner product is obtained by setting  $\ell = 0$  in (13) and the Riesz representers  $\nabla \chi_v(\varphi)$  and  $\nabla^{L^2} \chi_v(\varphi)$  are the gradients of the objective functional computed with respect to the  $H^1$  and  $L^2$  topology, respectively. We remark that, while the  $H^1$  gradient is used exclusively in the actual computations, cf. (14), the  $L^2$  gradient is computed first as an intermediate step.

However, we note that expression (15) for the Gâteaux differential is not yet consistent with the Riesz form (17), because the perturbation  $\varphi'$  of the initial data (1c) does not appear in it explicitly as a factor, but is instead hidden as the initial condition in the linearized problem, cf. (16b). In order to transform (15) to the Riesz form, we introduce the *adjoint states*  $\omega_v^*, \psi_v^* : \Omega \times [0, T] \rightarrow \mathbb{R}$  and the following duality-pairing relation

$$\left( \mathcal{K} \begin{bmatrix} \omega'_v \\ \psi'_v \end{bmatrix}, \begin{bmatrix} \omega_v^* \\ \psi_v^* \end{bmatrix} \right) := \int_0^T \int_\Omega \mathcal{K} \begin{bmatrix} \omega'_v \\ \psi'_v \end{bmatrix} \cdot \begin{bmatrix} \omega_v^* \\ \psi_v^* \end{bmatrix} d\mathbf{x} dt = 0. \tag{18}$$

Performing integration by parts with respect to both space and time in (18) and judiciously defining the *adjoint system* as (also subject to the period boundary conditions)

$$\begin{aligned} \mathcal{K}^* \begin{bmatrix} \omega_v^* \\ \psi_v^* \end{bmatrix} &:= \begin{bmatrix} -\frac{\partial \omega_v^*}{\partial t} - \nabla^\perp \psi_v \cdot \nabla \omega_v^* + \psi_v^* - \nu \Delta \omega_v^* \\ \Delta \psi_v^* - \nabla^\perp \cdot (\omega_v^* \nabla \omega_v) \end{bmatrix} \\ &= \begin{bmatrix} -\frac{2\nu}{T} \Delta \omega_v \\ 0 \end{bmatrix}, \end{aligned} \tag{19a}$$

$$\omega_v^*(t = T) = 0, \tag{19b}$$

we arrive at

$$\begin{aligned} &\left( \mathcal{K} \begin{bmatrix} \omega'_v \\ \psi'_v \end{bmatrix}, \begin{bmatrix} \omega_v^* \\ \psi_v^* \end{bmatrix} \right) \\ &= \left( \begin{bmatrix} \omega'_v \\ \psi'_v \end{bmatrix}, \mathcal{K}^* \begin{bmatrix} \omega_v^* \\ \psi_v^* \end{bmatrix} \right) - \int_\Omega \varphi'(\mathbf{x}) \omega_v^*(\mathbf{x}, 0) d\mathbf{x} \\ &= \underbrace{-\frac{2\nu}{T} \int_0^T \int_\Omega \omega'_v \Delta \omega_v d\mathbf{x} dt}_{\chi'_v(\varphi; \varphi')} - \int_\Omega \varphi'(\mathbf{x}) \omega_v^*(\mathbf{x}, 0) d\mathbf{x} = 0, \end{aligned} \tag{20}$$

where all boundary terms resulting from integration by parts with respect to the space variable vanish due to periodicity and one of the terms resulting from integration by parts with respect to time vanishes as well due to the terminal condition (19b). Identity (20) then implies  $\chi'_v(\varphi; \varphi') = \int_\Omega \varphi'(\mathbf{x}) \omega_v^*(\mathbf{x}, 0) d\mathbf{x}$ , from which we deduce the following expression for the  $L^2$  gradient, cf. (17),

$$\nabla^{L^2} \chi_v(\mathbf{x}) = \omega_v^*(\mathbf{x}, 0). \tag{21}$$

We note that the  $L^2$  gradient does not possess the regularity required to solve Problem 1. Identifying the Gâteaux differential (15) with the  $H^1$  inner product, cf. (13), integrating by parts and using (21), we obtain the required  $H^1$  gradient  $\nabla \chi$  as a solution of the elliptic boundary-value problem

$$[\text{Id} - \ell^2 \Delta] \nabla \chi_v = \nabla^{L^2} \chi_v \quad \text{in } \Omega, \tag{22}$$

subject to the periodic boundary conditions. As shown in [24], extraction of gradients in spaces of smoother functions such as  $H^1(\Omega)$  can be interpreted as low-pass filtering of the  $L^2$  gradients with parameter  $\ell$  acting as the cut-off length-scale. The value of  $\ell$  can significantly affect the rate of convergence of the iterative procedure (14).

We define the inverse Laplacian on  $\Omega$  such that it returns a zero-mean function. This ensures that the solution  $\omega_v^*$  of the adjoint system (19) preserves the zero-mean property which is then also inherited by the  $L^2$  and  $H^1$  gradients, cf. (21)–(22). The projection operator in (14) is then defined in terms of the normalization (retraction)

$$\mathbb{P}_S(\varphi) = \sqrt{\frac{\mathcal{P}_0}{\mathcal{P}(\varphi)}} \varphi. \tag{23}$$

An optimal step size  $\tau_n$  can be determined by solving the minimization problem

$$\tau_n = \arg \max_{\tau > 0} \left\{ \chi_v \left( \mathbb{P}_S \left( \varphi^{(n)} + \tau \nabla \chi_v(\varphi^{(n)}) \right) \right) \right\}, \tag{24}$$

which can be interpreted as a modification of a standard line search problem with optimization performed following an arc (a geodesic) lying on the constraint manifold  $S$ , rather than a straight line.

To summarize, a single iteration of the gradient algorithm (14) requires solution of the Navier–Stokes system (1) followed by the solution of the adjoint system (19), which is a terminal-value problem and hence needs to be integrated backward in time whereas its coefficients are determined by the solution of the Navier–Stokes system obtained before. These two solves allow one to evaluate the  $L^2$  gradient via (21) which is then “lifted” to the space  $H^1$  by solving (22). Finally, the approximation of the optimal initial condition  $\check{\varphi}_v^T$  is updated using (14) with the step size  $\tau_n$  determined in (24). As a first initial guess  $\varphi_0$  in (14) we use the initial condition constructed in [21] and then, to ensure the maximizers  $\check{\varphi}_v^T$  obtained for the same viscosity  $\nu$  but different lengths  $T$  of the time window lie on the same maximizing branch, we use a continuation approach where the maximizer  $\check{\varphi}_v^T$  is employed as the initial guess  $\varphi_0$  to compute  $\check{\varphi}_v^{T+\Delta T}$  for some sufficiently small  $\Delta T$ . In the same spirit, when searching for branches corresponding to different values of  $\nu$ , the maximizer  $\check{\varphi}_v^T$  is employed as the initial guess  $\varphi_0$  to find  $\check{\varphi}_v^{T+\Delta \nu}$  for some sufficiently small  $\Delta \nu$ . We refer the reader to [25] for further details of the continuation approach.

### 3.2. Computational approach

Both the Navier–Stokes (1) and the corresponding adjoint system (19) are discretized in space using a standard Fourier pseudo-spectral method. Evaluation of nonlinear products and terms with nonconstant coefficients is performed using the 2/3 rule

combined with a Gaussian filter defined by  $\rho(\mathbf{k}) = e^{-36 \left(\frac{|\mathbf{k}|}{K}\right)^{36}}$ , where  $\mathbf{k}$  is the wavenumber,  $K = \frac{2N}{3}$  and  $N$  is the number of Fourier modes used in each direction [26]. Time integration is carried out using a four-step, globally third-order accurate mixed implicit/explicit Runge–Kutta scheme with low truncation error [27]. The results presented in the next section were obtained using the spatial resolutions  $N = 512, 1024$  in each direction and the time-steps  $\Delta t \approx 4.4721 \times 10^{-5}, 2.2361 \times 10^{-5}, 8.9443 \times 10^{-6}$ , with finer resolutions employed for problems with smaller values of the viscosity  $\nu$ . In system (22) defining the Sobolev gradients we set  $\ell = 1$  and a spectral method is used to solve this system. The line-search problem (24) is solved with Brent’s derivative-free algorithm [28]. Due to its large computational cost, a massively parallel implementation of the approach presented has been developed in FORTRAN 90 using the Message Passing Interface (MPI).

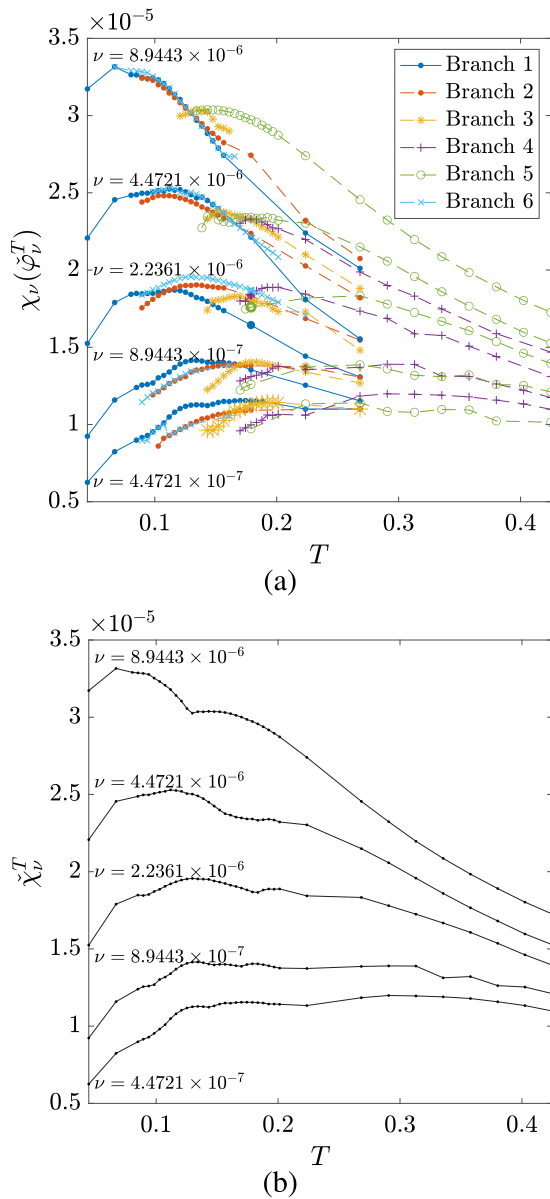


**Fig. 1.** Dependence of (a) the maximum enstrophy dissipation  $\chi_\nu(\tilde{\varphi}_\nu^T)$  for maximizers on the different branches, cf. Table 1, and (b) its envelope  $\tilde{\chi}_\nu^T$  on the length  $T$  of the time window for different viscosities  $\nu$ . In panel (a) the local maximizers illustrated in Table 1 are marked with larger symbols.

#### 4. Results

In this section we present the results obtained by solving Problem 1 with  $\mathcal{P}_0 = 1$  fixed and both  $\nu$  and  $T$  varying over a broad range of values. In addition to understanding the structure of the flows maximizing the enstrophy dissipation and how it changes when the parameters are varied, our goal is also to provide insights which of the estimates (7)–(11) best describe the behavior of the maximum enstrophy dissipation  $\chi_\nu(\tilde{\varphi}_\nu^T)$  in the limit of vanishing viscosity.

Problem 1 is nonconvex and as such admits multiple local maximizers at least for some values of  $\nu$  and  $T$ . The results are organized in terms of “branches” defined as families of optimal initial conditions  $\tilde{\varphi}_\nu^T$  obtained with fixed values of  $\nu$  and varying  $T$  such that the maximum enstrophy dissipation  $\chi_\nu(\tilde{\varphi}_\nu^T)$  is a smooth function of the length  $T$  of the time window. For each value of  $\nu$  and each branch, the time windows considered are then chosen to

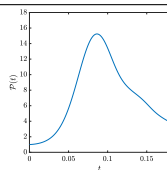
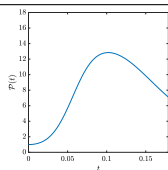
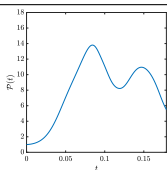
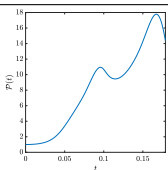
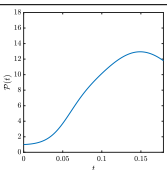
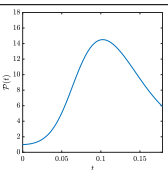
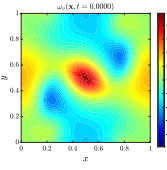
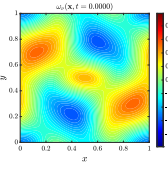
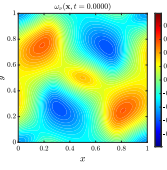
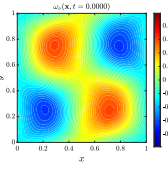
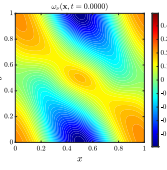
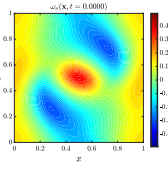
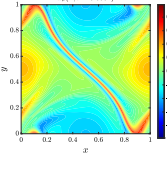
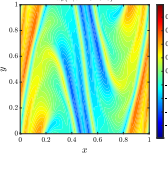
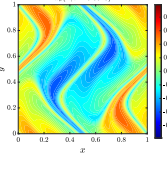
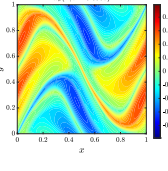
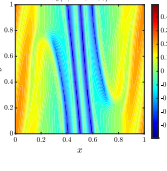
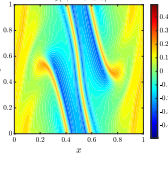
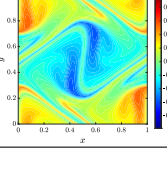
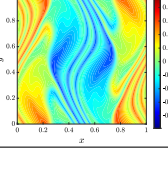
capture the local maximum of  $\chi_\nu(\tilde{\varphi}_\nu^T)$  and its neighborhood. Information about the local maximizers found for  $\nu = 2.2361 \times 10^{-6}$  and  $T = 0.1789$  on six distinct branches is collected in Table 1 where we show the corresponding palinstrophy evolutions  $\mathcal{P}(t)$ , optimal initial conditions  $\tilde{\varphi}_\nu^T(\mathbf{x})$  and the vorticity fields realizing the maximum palinstrophy  $\omega_\nu(\mathbf{x}, \arg \max_{0 < t \leq T} \mathcal{P}(t))$ . These branches were determined for the given value of  $\nu$  using the continuation approach described in Section 3.1 where  $\chi_\nu$  is regarded as a smooth function of  $T$ . When searching for branches corresponding to different viscosity values, continuation with respect to  $\nu$  with  $T$  fixed was also used. The time evolution of the vorticity fields corresponding to all six branches is visualized in Movie 1 [29]. This movie offers insights about the different physical mechanisms involving the stretching of thin vorticity filaments which are responsible for the growth of palinstrophy and hence also increased enstrophy dissipation. It is noteworthy that all these flow evolutions feature very thin filaments which however do not undergo the Kelvin–Helmholtz instability as they are stabilized by the shear induced by the large vortices also present in the flow field. This effect is well understood in the idealized setting of inviscid flows with straight vortex sheets [30], see also [31], and was observed in 2D turbulence [32]. Flows on branches 3 and 4, which feature multiple palinstrophy maxima, employ a mechanism similar to the continuous baker’s map to amplify the palinstrophy. Moreover, we see that, interestingly, in some cases seemingly very similar optimal initial conditions  $\tilde{\varphi}_\nu^T$  give rise to quite different flow evolutions featuring different numbers of local palinstrophy maxima (one or two) in the considered time window  $[0, T]$ , see, e.g., the maximizers from Branches 2 and 3 in Table 1. This makes classifying local optimizers into branches a rather difficult task and the classification presented in Table 1 is tentative only, which will however not affect the main findings of our study. Movies 2 [33] and 3 [34] show the flow evolutions and representative palinstrophy histories corresponding to the locally optimal initial conditions  $\tilde{\varphi}_\nu^T$  obtained, respectively, on Branch 1 with  $T = 0.1207$  and on Branch 5 with  $T = 0.2683$  for five different values of the viscosity  $\nu$ . In both cases we see that even though the optimal initial conditions  $\tilde{\varphi}_\nu^T$  obtained for different values of  $\nu$  are quite similar, qualitative changes occur in the flows evolutions as the viscosity is reduced. We attribute these changes to either possible bifurcations of the branches (understood as functions of  $\nu$ ) or to the possibility that the flow evolutions corresponding to smaller viscosity values belong to some unclassified branch, underpinning the difficulty mentioned above.

Next, in Fig. 1a we show the dependence of the maximum enstrophy dissipation  $\chi_\nu(\tilde{\varphi}_\nu^T)$  on the length  $T$  of the time window for five values of viscosity spanning more than one order of magnitude. We carefully distinguish branches of distinct local maximizers, where by a “branch” we mean a family of optimal initial data  $\tilde{\varphi}_\nu^T$  parametrized by  $T$  and such that the enstrophy dissipation  $\chi_\nu(\tilde{\varphi}_\nu^T)$  changes smoothly as  $T$  is varied while  $\nu$  remains fixed. We remark that for certain combinations of  $\nu$  and  $T$  only a subset of the local maximizers described in Table 1 could be found. In Fig. 1a we observe that along each branch the maximum enstrophy dissipation  $\chi_\nu(\tilde{\varphi}_\nu^T)$  admits a well-defined maximum with respect to  $T$ . We add that the values of  $\chi_\nu(\tilde{\varphi}_\nu^T)$  shown in Fig. 1a are for each value of  $\nu$  at least an order of magnitude larger than the enstrophy dissipation corresponding to the initial conditions constructed in [21], which realize the behavior given in (12).

As these are the quantities needed to make quantitative comparisons with estimates (7)–(11), in Fig. 1b we plot the “envelopes”, defined as  $\tilde{\chi}_\nu^T := \max_{\text{branches}} \chi_\nu(\tilde{\varphi}_\nu^T)$ , of the branches obtained at fixed values of  $\nu$ . “Singularities” evident in these curves correspond to values of  $T$  where different branches become dominant as  $T$  varies.

**Table 1**

Summary information about the local maximizers obtained by solving Problem 1 with  $\nu = 2.2361 \times 10^{-6}$  and  $T = 0.1789$ . The time evolution of the vorticity fields is visualized in Movie 1 [29]. “N/A” indicates that palinstrophy attains a single maximum only during the time evolution corresponding to the given branch.

Branch	1	2	3	4	5	6
Palinstrophy						
Initial condition						
Palinstrophy peak						
Palinstrophy peak 2	N/A	N/A			N/A	N/A

Next, we move on to identify quantitative connections between the data presented in Fig. 1b and estimates (7)–(11) describing the vanishing of the enstrophy dissipation in the inviscid limit  $\nu \rightarrow 0$ . These estimates also depend on the length  $T$  of the time window, but this dependence is in some cases less explicit and we will therefore consider  $T$  as a fixed parameter. We thus introduce the following ansätze

$$f_1(\nu) = C [-\ln(\nu)]^{-\frac{1}{2}}, \tag{25a}$$

$$f_2(\nu) = C \nu^\alpha, \tag{25b}$$

$$f_3(\nu) = C \left[ \frac{\nu}{|\ln(\nu)|} \right]^\alpha, \tag{25c}$$

$$f_4(\nu) = C \nu [-\ln(\nu)]^{\frac{1}{2}} \tag{25d}$$

motivated by the structure of the different estimates. More specifically, (25a) is the expression from Conjecture 1, cf. (7), (25b) has the general form of the upper bounds in (9)–(10), where in the latter case we only consider the second argument of the function  $\max(\cdot)$  since the function  $\phi_{\varphi,p,M}$  appearing in the first argument is not given explicitly enough to allow for quantitative comparisons, (25c) is motivated by the form of estimate (11) whereas (25d) is the bound from Theorem 1, cf. (12).

We want to find out which of the functions (25a)–(25d) best describes the dependence of the data shown in Fig. 1b on  $\nu$  for different fixed values of  $T$ . For each discrete value of  $T$  (marked with solid symbols in Fig. 1b) we determine the constant  $C = C(T)$  in each of the ansatz functions (25a)–(25d) by solving the problem

$$\tilde{C}(T) = \arg \min_{C \in \mathbb{R}^+} \mu_i^T(C), \quad i = 1, 2, 3, 4, \tag{26}$$

with the fitting error defined as

$$\mu_i^T(C) := \frac{1}{5} \sum_{j=1}^5 \left| \tilde{\chi}_{\nu_j}^T - f_i(\nu_j; C) \right|, \tag{27}$$

where  $\nu_j \in \{8.9443 \times 10^{-6}, 4.4721 \times 10^{-6}, 2.2361 \times 10^{-6}, 8.9443 \times 10^{-7}, 4.4721 \times 10^{-7}\}$  are the considered values of the viscosity. The fitting error (27) will be used to measure the accuracy with which the different ansatz functions (25a)–(25d) represent the data. In addition, we note that ansatz functions (25b)–(25c) also involve a priori undefined exponents  $\alpha \in (0, 1)$ . To determine this additional parameter in  $f_2$  and  $f_3$ , we embed problem (26) in a bracketing procedure which finds the exponent  $\tilde{\alpha} = \tilde{\alpha}(T)$  producing the smallest fitting error (27) for a given value of  $T$ . This bracketing procedure is performed by first determining  $\mu_i^T(\tilde{C}(T))$ , by solving problem (26), for a range of discrete values of  $\alpha \in [0, 1]$  and then using bisection to iteratively improve the approximation of  $\tilde{\alpha} = \tilde{\alpha}(T)$  which produces the smallest error (27). We emphasize that even though the ansätze (25a)–(25d) involve different numbers of parameters (one or two), they are all fitted to the data in Fig. 1b in the same way (i.e., by adjusting  $C = C(T)$ ), which is done independently for different discrete exponents  $\alpha$  in the case of relations (25b)–(25c).

In order to assess now well the different ansatz functions (25a)–(25d) capture the dependence of the maximum enstrophy dissipation  $\tilde{\chi}_\nu^T$  on  $\nu$ , cf. Fig. 1b, we define the ratios  $\tilde{\chi}_\nu^T / f_i(\nu)$ ,  $i = 1, 2, 3, 4$ , and plot them as functions of  $\nu$  for different  $T$  in Figs. 2a–d using the values of  $\tilde{C} = \tilde{C}(T)$  and  $\tilde{\alpha} = \tilde{\alpha}(T)$  determined as above. Thus, if  $\tilde{\chi}_\nu^T / f_i(\nu)$  is close to unity over the entire range of  $\nu$ , this signals that the ansatz function  $f_i(\nu)$  accurately captures the dependence of  $\tilde{\chi}_\nu^T$  on  $\nu$  for the given value of  $T$ . We see that this is what indeed happens for  $f_2(\nu)$  and  $f_3(\nu)$  for most values of  $T$ , cf. Figs. 2b, c. On the other hand, we note that relations  $f_1(\nu)$  and  $f_4(\nu)$ , respectively, overestimate and underestimate the actual dependence of  $\tilde{\chi}_\nu^T$  on  $\nu$ , cf. Figs. 2a, d. This observation is consistent with the fact that (25a) represents estimate (7), which is more conservative than bounds (9)–(11), and (25d) has the form of the lower bound (12).

Hereafter we will focus on the fits given in terms of ansatz functions (25b)–(25c). In order to decide which of these relations

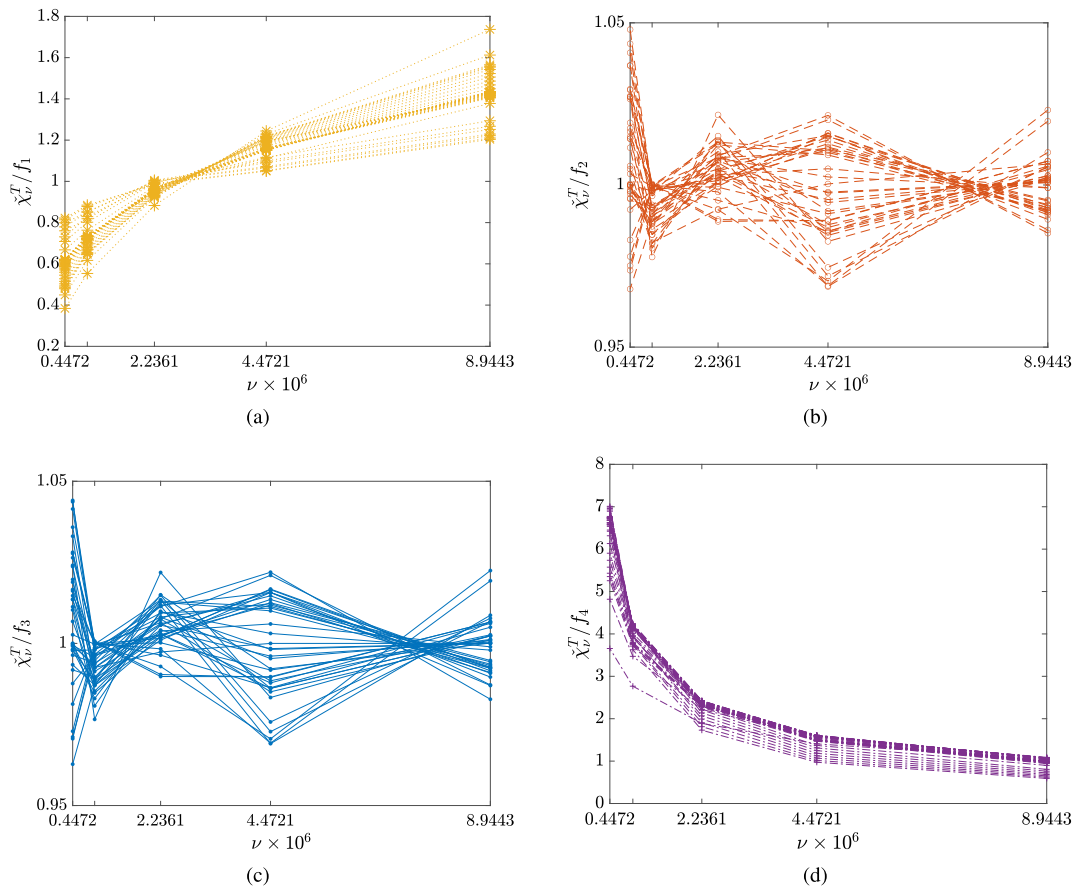


**Fig. 2.** Dependence of (a)  $\tilde{\chi}_v^T/f_1(\nu)$ , (b)  $\tilde{\chi}_v^T/f_2(\nu)$ , (c)  $\tilde{\chi}_v^T/f_3(\nu)$  and (d)  $\tilde{\chi}_v^T/f_4(\nu)$ , with optimal constants  $\tilde{C} = \tilde{C}(T)$  and exponents  $\tilde{\alpha} = \tilde{\alpha}(T)$ , on the viscosity  $\nu$  for different  $T$ .

more accurately represents the dependence of  $\tilde{\chi}_v^T$  on  $\nu$ , in Fig. 3 we show the corresponding fitting errors (27) as functions of  $T$ . Smaller fitting errors  $\mu_i^T(\tilde{C}(T))$  indicate a better fit between the ansatz function  $f_2$  or  $f_3$  and the data  $\tilde{\chi}_v^T$  for the given value of  $T$ . We see that relation  $f_2(\nu)$  generally leads to smaller errors for shorter time windows (with  $T \leq 0.147$ ), whereas relation  $f_3(\nu)$  tends to better predict the dependence of  $\tilde{\chi}_v^T$  on  $\nu$  for longer time windows. Finally, the optimal exponents  $\tilde{\alpha} = \tilde{\alpha}(T)$  determined for ansatz functions (25b)–(25c) are shown in Fig. 4 where an overall decreasing trend with  $T$  is evident. As regards the “dip” occurring for  $0.0894 \lesssim T \lesssim 0.1342$ , we speculate that it may be the result of some branches not being captured in Fig. 1a. We note that, remarkably, the dependence of the exponent  $\tilde{\alpha}$  on  $T$  reveals an approximately exponential form consistent with the structure of the upper bounds in (10)–(11), more specifically, the exponential dependence of the exponents of  $\nu$  in these bounds on  $T$ . Moreover, the limit  $\lim_{T \rightarrow 0} \tilde{\alpha}(T)$  is also quantitatively consistent with predictions of estimate (11).

### 5. Summary and conclusions

In this study we provide a quantitative characterization of the behavior of the enstrophy dissipation in 2D Navier–Stokes flows in the limit of vanishing viscosity. Unlike the case of Burgers flows in 1D and Navier–Stokes flows in 3D where the energy dissipation anomaly is well documented, 2D Navier–Stokes flows are known not to exhibit anomalous behavior of enstrophy dissipation. As discussed in Introduction, the vanishing of enstrophy dissipation in the inviscid limit is subject to various estimates, some ad-hoc and some rigorous, providing lower and upper bounds on this quantity as viscosity vanishes. In our investigation we have

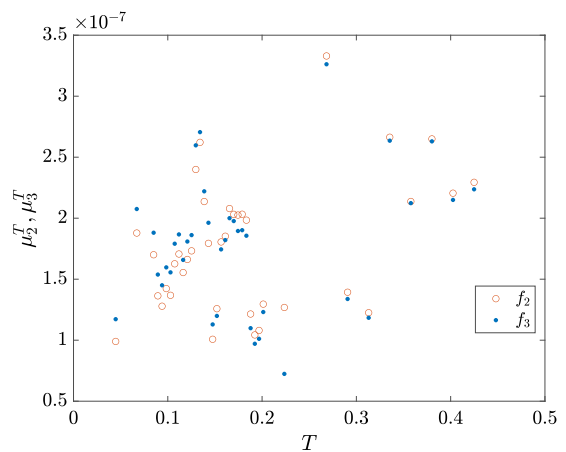


**Fig. 3.** Dependence of the fitting errors  $\mu_i^T(\tilde{C}(T))$ ,  $i = 2, 3$ , cf. (27), corresponding to the ansatz functions (red circles)  $f_2(\nu)$  and (blue dots)  $f_3(\nu)$  to  $\tilde{\chi}_v^T$  for different  $T$ .

probed the sharpness of these estimates by constructing families of Navier–Stokes flows designed to locally maximize the enstrophy dissipation subject to certain constraints. This was done by solving Problem 1 where locally optimal initial data  $\tilde{\varphi}_v^T$  with fixed palinstrophy  $\mathcal{P}_0$  was found such that the corresponding flow with the given viscosity  $\nu$  maximizes the enstrophy dissipation  $\chi_\nu$  over the time window  $[0, T]$ . Problem 1 was solved numerically using a state-of-the-art adjoint-based gradient ascent method described in Section 3. This optimization problem is nonconvex

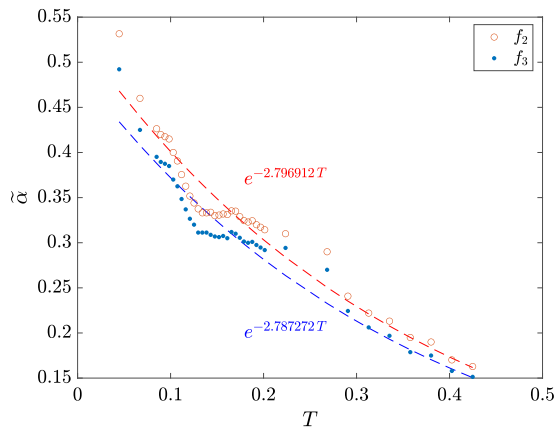


**Fig. 4.** Dependence of the optimal exponents  $\tilde{\alpha} = \tilde{\alpha}(T)$  in the ansatz functions (red circles)  $f_2(\nu)$  and (blue dots)  $f_3(\nu)$  on the length  $T$  of the time window. The dashed lines represent exponential fits, in the forms indicated, to the values of  $\tilde{\alpha} = \tilde{\alpha}(T)$  for the ansatz function (red)  $f_2(\nu)$  and (blue)  $f_3(\nu)$ .

and we have found six distinct branches of local maximizers, each associated with a different mechanism for palinstrophy amplification, cf. Table 1. As is evident from Movie 1 [29], while in all cases palinstrophy amplification involves stretching of thin vorticity filaments, there are multiple ways to design flows maximizing this process on a periodic domain  $\Omega$  and which of these different mechanisms produces the largest enstrophy dissipation depends on the value of viscosity  $\nu$  and the length  $T$  of the time window, cf. Fig. 1a.

Branches of local maximizers found by solving Problem 1 for different values of  $\nu$  and  $T$  reveal how the extreme behavior of the enstrophy dissipation they realize compares with the available estimates on this process discussed in Introduction. We conclude that the dependence of the maximum enstrophy dissipation  $\check{\chi}_\nu^T$  in the extreme flows we found on  $\nu$  with fixed  $T$  is quantitatively consistent with the upper bound in estimate (10), cf. Fig. 2b, which is the sharpest estimate available to date. Remarkably, the exponential dependence of the exponent in this upper bound on  $T$  is also quantitatively consistent with our results, cf. Fig. 4 (we attribute the deviation from the exponential decrease evident around  $T \approx 0.1342$  in this figure to the likely possibility that, despite our efforts, not all branches of maximizing solutions have been found).

As regards estimate (10), we note that it depends on the quantity  $\|\check{\varphi}_\nu^T\|_{L^\infty(\Omega)}$  (via the constant  $M$ ). Since our optimal initial conditions are sought in the space  $H^1(\Omega)$ , we do not have an a priori control over this quantity, however, in our computations we did not find any evidence for  $\|\check{\varphi}_\nu^T\|_{L^\infty(\Omega)}$  to attain large values. Thus, these caveats notwithstanding, we conclude that estimate (10) is sharp and does not offer any room for improvement, other than perhaps a logarithmic correction analogous to the one appearing in (11). Relation (11) was found to describe the dependence of the maximum enstrophy dissipation  $\check{\chi}_\nu^T$  on viscosity in the limit  $\nu \rightarrow 0$  with similar accuracy to estimate (10). However, we reiterate that, as discussed in Introduction, (11) does not represent a rigorous upper bound on the enstrophy dissipation. Improving this estimate, so that the  $\dot{H}^{-1}(\Omega)$  norm on the left-hand side in (11) is strengthened to  $L^2(\Omega)$ , appears to be an open question in mathematical analysis.

Among other open problems, it would be interesting to better understand the bifurcation structure of the different optimal solution branches shown in Fig. 1a. Another open question is what new insights about the problem considered here could be deduced based on the kinetic theory, i.e., by considering an

optimization problem analogous to Problem 1 in the context of the Boltzmann equation or some of its variants. Some efforts in this direction are already underway. Finally, there is the question about what can be said about the energy dissipation anomaly in 3D Navier–Stokes flows using the approach developed in the present study.

### Declaration of competing interest

The authors declare that they have no known competing financial interests or personal relationships that could have appeared to influence the work reported in this paper.

### Acknowledgments

This work is dedicated to the memory of the late Charlie Doering, our dear friend and collaborator, who served as an inspiration to so many of us. It is related to our long-term research program influenced by Charlie's interest in questions concerning saturation of rigorous bounds.

The authors thank Roman Shvydkoy for interesting discussions and for bringing a number of relevant references to their attention.

The first two authors acknowledge the support through an NSERC (Canada) Discovery Grant. The second author would like to thank the Isaac Newton Institute for Mathematical Sciences for support and hospitality during the programme “Mathematical aspects of turbulence: where do we stand?” where this work was finalized. This work was supported by EPSRC, United Kingdom grant number EP/R014604/1. The research of the third author was partly supported by the JSPS Grants-in-Aid for Scientific Research 20H01819. The authors also thank the Japan Society for the Promotion of Science for awarding the first author a research fellowship to conduct this work. Computational resources were provided by Compute Canada under its Resource Allocation Competition.

### Appendix A. Supplementary data

Supplementary material related to this article can be found online at <https://doi.org/10.1016/j.physd.2022.133517>.

### References

- [1] U. Frisch, *Turbulence*, Cambridge University Press, Cambridge, 1995, <http://dx.doi.org/10.1017/CBO9781139170666>, The legacy of A. N. Kolmogorov.
- [2] K.R. Sreenivasan, An update on the energy dissipation rate in isotropic turbulence, *Phys. Fluids* 10 (2) (1998) 528–529, <http://dx.doi.org/10.1063/1.869575>.
- [3] P.K. Yeung, X.M. Zhai, K.R. Sreenivasan, Extreme events in computational turbulence, *Proc. Natl. Acad. Sci.* 112 (41) (2015) 12633–12638, <http://dx.doi.org/10.1073/pnas.1517368112>, arXiv:https://www.pnas.org/doi/pdf/10.1073/pnas.1517368112. URL <https://www.pnas.org/doi/pdf/10.1073/pnas.1517368112>.
- [4] R. Dascaliuc, Z. Grujić, Anomalous dissipation and energy cascade in 3D inviscid flows, *Comm. Math. Phys.* 309 (3) (2012) 757–770.
- [5] K.R. Sreenivasan, Turbulent mixing: A perspective, *Proc. Natl. Acad. Sci.* 116 (37) (2019) 18175–18183, <http://dx.doi.org/10.1073/pnas.1800463115>, arXiv:https://www.pnas.org/doi/pdf/10.1073/pnas.1800463115. URL <https://www.pnas.org/doi/pdf/10.1073/pnas.1800463115>.
- [6] A. Mazzucato, Remarks on anomalous dissipation for passive scalars, *Phil. Trans. R. Soc. A* 380 (2218) (2022) 20210099, <http://dx.doi.org/10.1098/rsta.2021.0099>, arXiv:https://royalsocietypublishing.org/doi/pdf/10.1098/rsta.2021.0099. URL <https://royalsocietypublishing.org/doi/pdf/10.1098/rsta.2021.0099>.
- [7] G.L. Eyink, T.D. Drivas, Spontaneous stochasticity and anomalous dissipation for Burgers equation, *J. Stat. Phys.* 158 (2) (2015) 386–432, <http://dx.doi.org/10.1007/s10955-014-1135-3>.
- [8] G.K. Batchelor, Computation of the energy spectrum in homogeneous two-dimensional turbulence, *Phys. Fluids* 12 (12) (1969) II–233–239, <http://dx.doi.org/10.1063/1.1692443>, arXiv:https://aip.scitation.org/doi/pdf/10.1063/1.1692443. URL <https://aip.scitation.org/doi/abs/10.1063/1.1692443>.

- [9] C.V. Tran, D.G. Dritschel, Vanishing enstrophy dissipation in two-dimensional Navier–Stokes turbulence in the inviscid limit, *J. Fluid Mech.* 559 (2006) 107–116, <http://dx.doi.org/10.1017/S0022112006000577>.
- [10] M. Filho, A. Mazzucato, H. Nussenzveig Lopes, Weak solutions, renormalized solutions and enstrophy defects in 2D turbulence, *Arch. Ration. Mech. Anal.* 179 (3) (2006) 353–387, <http://dx.doi.org/10.1007/s00205-005-0390-5>.
- [11] M.D. Gunzburger, *Perspectives in Flow Control and Optimization*, SIAM, 2003, <http://dx.doi.org/10.1137/1.9780898718720>, arXiv:<https://epubs.siam.org/doi/pdf/10.1137/1.9780898718720>. URL <https://epubs.siam.org/doi/abs/10.1137/1.9780898718720>.
- [12] B. Protas, Systematic search for extreme and singular behaviour in some fundamental models of fluid mechanics, *Phil. Trans. R. Soc. A* 380 (2225) (2022) 20210035, <http://dx.doi.org/10.1098/rsta.2021.0035>, arXiv:<https://royalsocietypublishing.org/doi/pdf/10.1098/rsta.2021.0035>. URL <https://royalsocietypublishing.org/doi/abs/10.1098/rsta.2021.0035>.
- [13] D. Ayala, B. Protas, Maximum palinstrophy growth in 2D incompressible flows, *J. Fluid Mech.* 742 (2014) 340–367.
- [14] D. Ayala, B. Protas, Vortices, maximum growth and the problem of finite-time singularity formation, *Fluid Dyn. Res.* 46 (3) (2014) 031404.
- [15] D. Ayala, C.R. Doering, T.M. Simon, Maximum palinstrophy amplification in the two-dimensional Navier–Stokes equations, *J. Fluid Mech.* 837 (2018) 839–857, <http://dx.doi.org/10.1017/jfm.2017.874>.
- [16] H. Kreiss, J. Lorenz, *Initial–Boundary Value Problems and the Navier–Stokes Equations*, Vol. 47 of *Classics in Applied Mathematics*, SIAM, 2004.
- [17] P. Constantin, T.D. Drivas, T.M. Elgindi, Inviscid limit of vorticity distributions in the Yudovich class, *Comm. Pure Appl. Math.* 75 (1) (2022) 60–82, <http://dx.doi.org/10.1002/cpa.21940>, arXiv:<https://onlinelibrary.wiley.com/doi/pdf/10.1002/cpa.21940>. URL <https://onlinelibrary.wiley.com/doi/abs/10.1002/cpa.21940>.
- [18] G. Ciampa, G. Crippa, S. Spirito, Strong convergence of the vorticity for the 2D Euler equations in the inviscid limit, *Arch. Ration. Mech. Anal.* 240 (1) (2021) 295–326, <http://dx.doi.org/10.1007/s00205-021-01612-z>.
- [19] H.J.N. Lopes, C. Seis, E. Wiedemann, On the vanishing viscosity limit for 2D incompressible flows with unbounded vorticity, *Nonlinearity* 34 (5) (2021) 3112–3121, <http://dx.doi.org/10.1088/1361-6544/abe51f>.
- [20] C. Seis, A note on the vanishing viscosity limit in the Yudovich class, *Canad. Math. Bull.* 64 (1) (2021) 112–122, <http://dx.doi.org/10.4153/S0008439520000296>.
- [21] I.-J. Jeong, T. Yoneda, Enstrophy dissipation and vortex thinning for the incompressible 2D Navier–Stokes equations, *Nonlinearity* 34 (4) (2021) 1837–1853, <http://dx.doi.org/10.1088/1361-6544/abd52d>.
- [22] A. Alexakis, C.R. Doering, Energy and enstrophy dissipation in steady state 2D turbulence, *Phys. Lett. A* 359 (6) (2006) 652–657, <http://dx.doi.org/10.1016/j.physleta.2006.07.048>, URL <https://www.sciencedirect.com/science/article/pii/S0375960106011728>.
- [23] D. Luenberger, *Optimization by Vector Space Methods*, John Wiley and Sons, 1969.
- [24] B. Protas, T.R. Bewley, G. Hagen, A computational framework for the regularization of adjoint analysis in multiscale PDE systems, *J. Comput. Phys.* 195 (1) (2004) 49–89, <http://dx.doi.org/10.1016/j.jcp.2003.08.031>, URL <http://www.sciencedirect.com/science/article/pii/S0021999103005114>.
- [25] D. Ayala, B. Protas, Extreme vortex states and the growth of enstrophy in 3D incompressible flows, *J. Fluid Mech.* 818 (2017) 772–806.
- [26] T.Y. Hou, Blow-up or no blow-up? A unified computational and analytic approach to 3D incompressible Euler and Navier–Stokes equations, *Acta Numer.* 18 (2009) 277–346, <http://dx.doi.org/10.1017/S0962492906420018>.
- [27] R. Alimo, D. Cavaglieri, P. Beyhaghi, T.R. Bewley, Design of IMEXRK time integration schemes via delaunay-based derivative-free optimization with nonconvex constraints and grid-based acceleration, *J. Global Optim.* 79 (3) (2021) 567–591, <http://dx.doi.org/10.1007/s10898-019-00855-1>.
- [28] W.H. Press, S.A. Teukolsky, W.T. Vetterling, B.P. Flannery, *Numerical Recipes*, third ed., Cambridge University Press, 2007, the art of scientific computing.
- [29] See Movie 1 for supplementary video.
- [30] M. Kiya, M. Arie, Helmholtz instability of a vortex sheet in uniform shear flow, *Phys. Fluids* 22 (2) (1979) 378–379, <http://dx.doi.org/10.1063/1.862590>, arXiv:<http://aip.scitation.org/doi/pdf/10.1063/1.862590>. URL <http://aip.scitation.org/doi/abs/10.1063/1.862590>.
- [31] T. Sakajo, H. Okamoto, Numerical computation of vortex sheet roll-up in the background shear flow, *Fluid Dyn. Res.* 17 (1996) 195–212.
- [32] N.K.-R. Kevlahan, M. Farge, Vorticity filaments in two-dimensional turbulence: Creation, stability and effect, *J. Fluid Mech.* 346 (1997) 49–76, <http://dx.doi.org/10.1017/S0022112097006113>.
- [33] See Movie 2 for supplementary video.
- [34] See Movie 3 for supplementary video.